BBAA VI International Colloquium on:
Bluff Bodies Aerodynamics & Applications
Milano, Italy, July, 20-24 2008

WIND LOADS ON OPEN-TOPPED OIL STORAGE TANKS

Yasushi Uematsu[*], Choongmo Koo[†], and Koji Kondo[††]

[*] Department of Architecture and Building Science, Tohoku University, Sendai 980-8579, Japan
e-mail: yu@venus.str.archi.tohoku.ac.jp

[†] Department of Architecture and Building Science, Tohoku University, Sendai 980-8579, Japan
e-mail: koo@venus.str.archi.tohoku.ac.jp

[††] Kajima Techinical Research Institute, Chohu 182-0036, Japan
e-mail: kondokoj@kajima.com

Keywords: Open-topped Tank, Thin Circular Cylindrical Shell, Wind Tunnel Experiment, Wind Load, POD Analysis, Conditional Sampling, Buckling.

1 INTRODUCTION

Wind loads and aerodynamic behavior of circular cylindrical structures, such as oil-storage tanks and silos, were studied extensively in the past (e.g. MacDonald et al. [1, 2], Holroyd [3], Uematsu et al. [4, 5], Uchiyama et al. [6]). However, no study has been made of the dynamic wind forces based on simultaneous pressure measurements at many locations both on the external and internal surfaces of open-topped cylinders in turbulent boundary layers. In such structures, wind load becomes the most critical when they are empty. Design wind loads are usually determined based on the time-averaged wind pressure distributions on the external and internal surfaces. However, the wind loads should be evaluated by considering the dynamic load effects and the correlation between the external and internal pressures.

The present paper discusses the design wind loads on open-topped oil storage tanks, based on wind pressure measurements with rigid models in a turbulent boundary layer as well as on experimental and theoretical analyses of the buckling behavior of thin cylindrical shells under wind loading. Two series of wind tunnel experiments are carried out. In the first series, simultaneous pressure measurements both on the external and internal surfaces of the wall are made. The pressures on the floating roof at various heights are also measured; however, focus is on the empty condition in the present paper. A conditional sampling technique and a POD (Proper Orthogonal Decomposition) analysis are employed to understand the characteristics of pressure field on the wall in detail. In the second series of experiments, the buckling behavior of thin cylindrical shells with or without roof is investigated both experimentally and theoretically. A special attention is paid to the critical wind force per unit area at the windward stagnation point causing a buckling of the shell. The buckling load obtained from the wind tunnel experiment is compared with those from a theoretical analysis as well as from an empirical formula that was proposed for longer cylinders with closed top (Uematsu and Uchiyama [5]).

2 WIND PRESSURE DISTRIBUTIONS ON RIGID MODELS

2.1 Experimental apparatus and procedures

Figure 1 shows the experimental setup and a model for pressure measurements. The wind-tunnel experiments were carried out in a closed-circuit-type wind tunnel at Kajima Technical Research Institute, which has a working section 18.1 m long, 2.5 m wide and 2.0 m high. A turbulent boundary layer with a power law exponent of approximately 0.15 was generated on the wind tunnel floor (see Figure 1(a)). The turbulence intensity I_u is approximately 0.16 at a height of z = 125 mm and 0.14 at z = 250 mm. The geometric scale of wind-tunnel flow is approximately 1/400. Two models (Models A and B) with smooth surface are used in the experiments. The dimensions of the models and the tap location are shown in Figure 2. The external diameter (D) is 250 mm. The aspect ratio (H/D) is 0.5 for Model A and 1.0 for Model B. The wall thickness is 6 mm for both models. The pressure taps of 0.5 mm diameter are installed at a step of 15^o on the external surface and at a step of 30^o on the internal surface along each circumference. The roof height h_r can be varied from 0 to H. Ninety-seven pressure taps are installed on the roof, as shown in Figure 2(c).

The pressure taps are connected to pressure transducers in parallel via 80 cm lengths of flexible vinyl tubing of 1 mm inside diameter. The wind pressures at all pressure taps are sampled at a rate of 1 kHz for approximately 33 sec simultaneously. The compensation for the frequency response of the pneumatic tubing system is carried out by using a digital filter to obtain a flat response up to about 500 Hz. The wind velocity U_H at $z = H$ is approximately 10 m/s for both models; the corresponding Reynolds number Re ($=U_H D/\nu$, with ν being the kinematic viscosity of the air) is approximately 1.6×10^5. The Reynolds number regime is regarded as 'transcritical', based on McDonald et al. [1] and Uematsu and Koo [7].

(a) Experimental setup (b) Model A (h_r =0)

Figure 1: Experimental setup and model for pressure measurements (Model A).

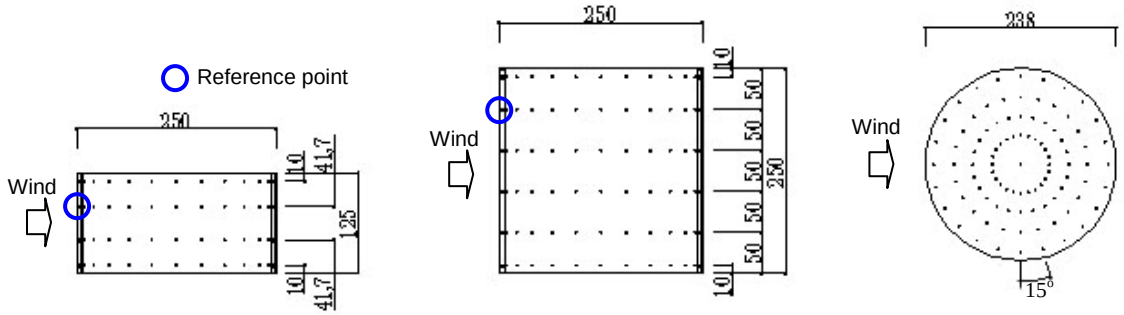

(a) Model A (H/D = 0.5) (b) Model B (H/D = 1.0) (c) Roof

Figure 2: Dimensions of wind-tunnel models and location of pressure taps (external wall surface and roof).

2.2 Results and discussion

2.2.1 Statistics of wind pressures

The mean, standard deviation (RMS), the maximum and minimum peak pressure coefficients ($C_{p\text{mean}}$, $C_{p\text{rms}}$, $C_{p\text{max}}$, $C_{p\text{min}}$) at all pressure taps are first computed. The same statistical values ($C_{f\text{mean}}$, $C_{f\text{rms}}$, $C_{f\text{max}}$, $C_{f\text{min}}$) of the net wind force (pressure difference) coefficients C_f on the wall are also computed. Since the internal wall pressures were measured at a step of 30° in the circumferential direction, the wind pressure coefficients at the mid points are interpolated by using the cubic spline function. Wind pressure and force coefficients are defined in terms of the dynamic pressure q_H of the approaching flow at $z = H$. Note that each statistical value is evaluated by the ensemble average of the results of five or six consecutive runs, each of which corresponds to a period of 10 min in full scale.

Figure 3 shows the distributions of $C_{p\text{mean}}$ and $C_{f\text{mean}}$, represented by contour lines, on the wall when $h_r = 0$ (empty condition). Furthermore, the circumferential distributions of $C_{f\text{mean}}$ at various heights are shown in Figure 4; the solid line in the figure represents the average over the whole height ($z = 0 - H$), which will be used for the buckling analysis in Chapter 3. Positive pressures are induced in the windward region. The external wind pressure coefficient along the windward generator increases with height and attains the maximum at $z \approx 2/3H$ for Model A and at $z \approx 4/5H$ for Model B; then, it decreases with height. The same feature is observed for $C_{f\text{mean}}$. The variation of $C_{p\text{mean}}$ on the external surface with height is not significant in the side and leeward regions. The value of $C_{p\text{mean}}$ on the internal surface changes only slightly both in the vertical and circumferential directions.

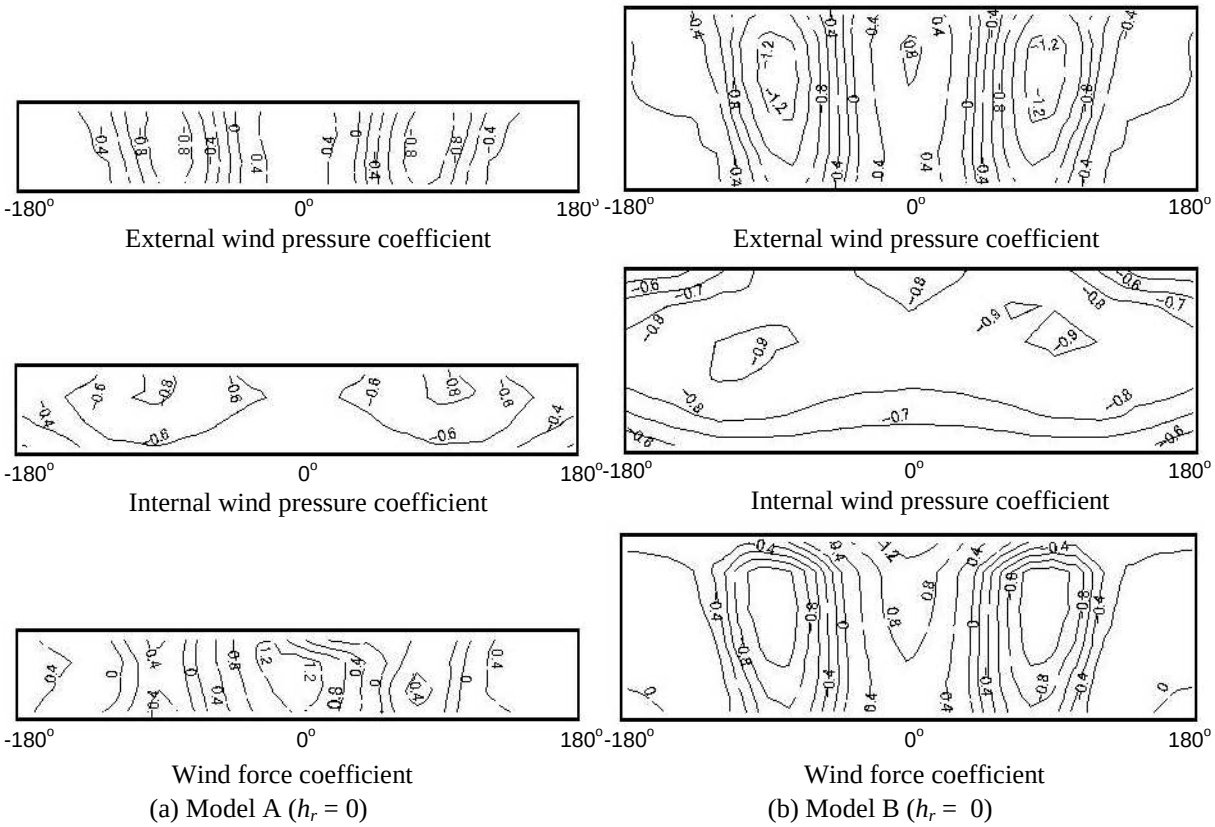

Figure 3: Distributions of $C_{p\text{mean}}$ and $C_{f\text{mean}}$ on the wall.

Figure 5 shows the circumferential distributions of the statistical values of the pressure coefficient C_p along a circumference at $z = 2/3H$ for Model A when $h_r = 0$. The distributions

of $C_{p\max}$ and $C_{p\min}$ are similar to that of $C_{p\mathrm{mean}}$. An instantaneous C_p-distribution can take place over a wide range from the $C_{p\max}$- to the $C_{p\min}$-curve. Therefore, the spatial correlation of wind pressures should be taken into account when discussing the design wind loads. The $C_{p\mathrm{rms}}$ value does not change significantly in the circumferential direction.

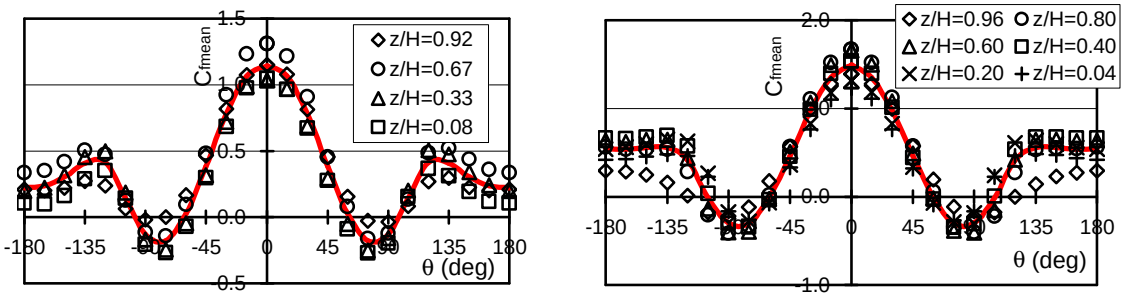

(a) Model A (h_r = 0) (b) Model B (h_r = 0)

Figure 4: Circumferential distributions of the mean wind force coefficient at various heights.

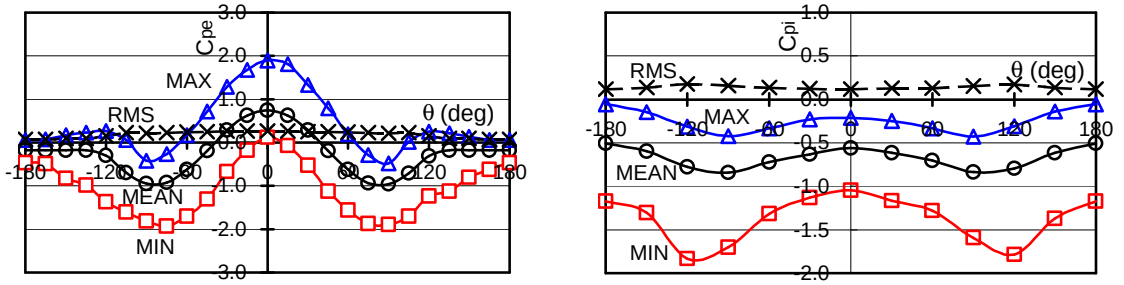

(a) External wind pressure coefficient (b) Internal wind pressure coefficient

Figure 5: Distributions of the external and internal pressure coefficients at $z = 2/3H$ (Model A, h_r=0).

The distributions of $C_{p\mathrm{mean}}$ on the floating roof at various heights h_r are shown in Figure 6. The roof is generally subjected to suctions. The distribution of $C_{p\mathrm{mean}}$ becomes more uniform with a decrease in h_r. Figure 7 shows the spatially averaged values of $C_{p\mathrm{mean}}$ over the roof and internal wall surface, plotted as a function of h_r/H. These values decrease in magnitude with an increase in h_r/H. However, the effect of h_r is not significant, particularly for the roof pressure. A similar feature was observed for longer cylinders (see Uematsu and Koo [7]).

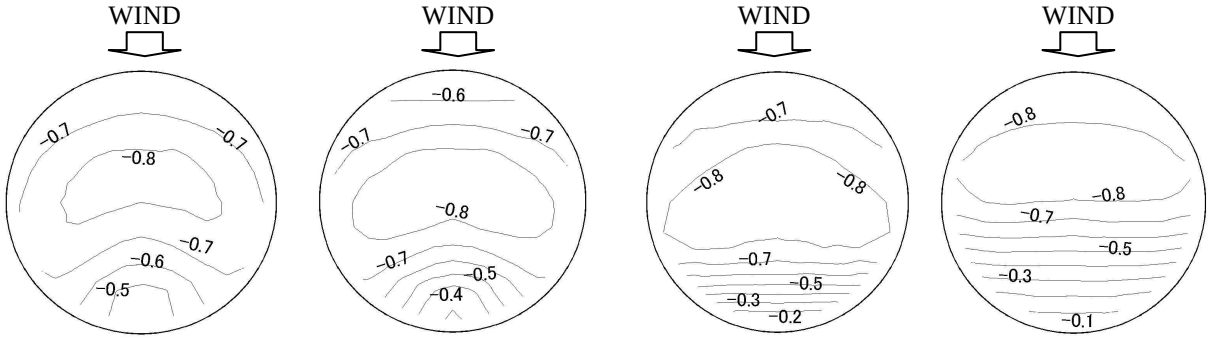

(a) h_r = 0 (b) h_r = 0. 29 (c) h_r = 0.71 (d) h_r = 0.96

Figure 6: Distributions of the mean pressure coefficients on the floating roof (Model B).

Figures 8 and 9 show the distributions of the correlation coefficients R between the wind pressures at a reference point (see Figure 1) and the other points on the wall. It is interesting to note that the distribution of R is similar in shape to that of C_{pmean}, particularly in the windward positive-pressure region. In the wake region, however, the magnitude of R is rather small, nearly equal to zero. The value of R on the internal surface does not change significantly except for the regions near the top and bottom; it is approximately -0.5 for Model A and -0.7 to -0.6 for Model B.

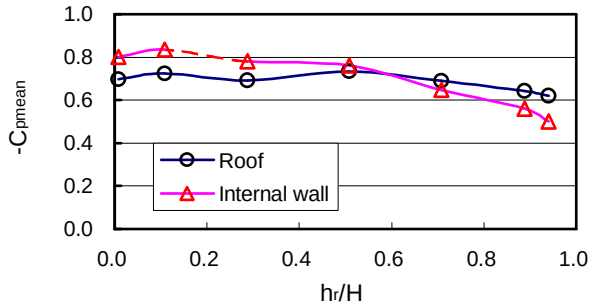

Figure 7: Spatially averaged values of C_{pmean} over the roof and internal wall surface (Model B).

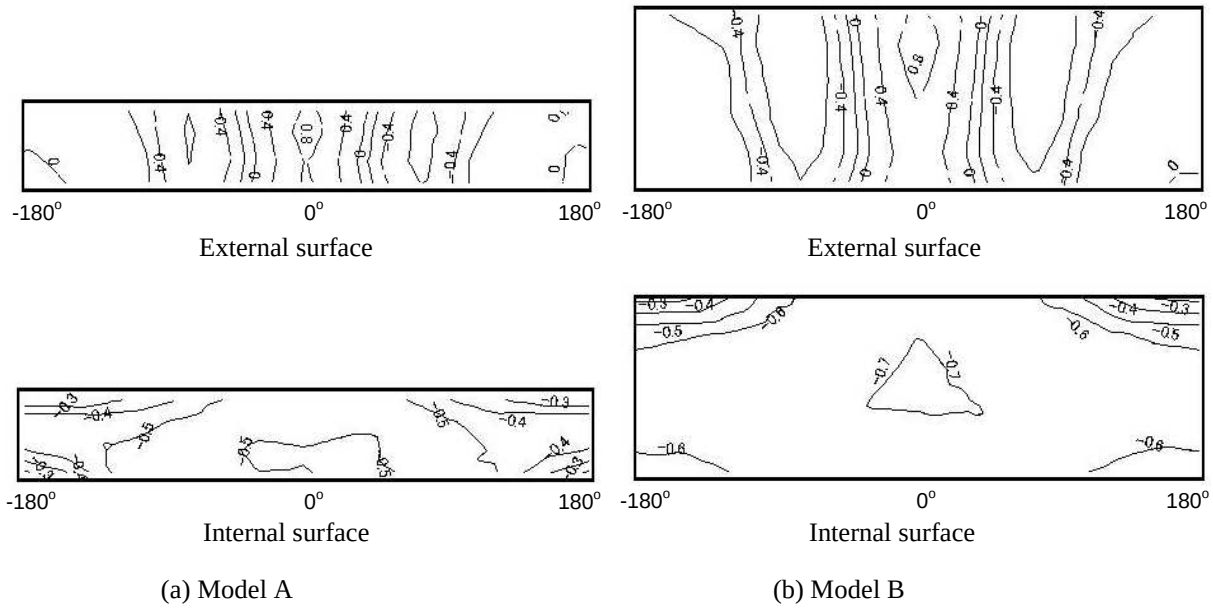

(a) Model A (b) Model B

Figure 8: Distributions of the correlation coefficient of pressures on the external and internal wall surfaces.

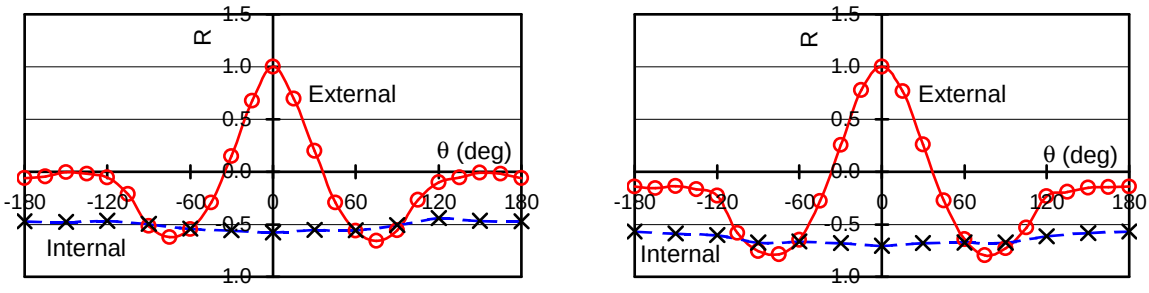

(a) Model A (z = 2/3H) (b) Model B (z = 4/5H)

Figure 9: Circumferential distribution of the correlation coefficient of pressures.

2.2.2 Conditional sampling

Uematsu and Uchiyama [5] indicated that the buckling behavior of thin cylindrical shells under wind loading is dependent on the extent of positive pressures as well as on the magnitude of the maximum pressure. Therefore, the pressure distribution at the instant t_{max} when the external wind pressure at the reference point becomes the maximum peak value may be very important from the viewpoint of structural stability of the shell, particularly for open-topped tanks. To investigate such a pressure distribution, a conditional sampling of wind pressures was carried out. Figures 10 and 11 show sample results; the pressure coefficient distributions along a circumference at z = 2/3H (Model A) or at z = 4/5H (Model B) are plotted in Figure 11. The instantaneous C_p value at $t = t_{max}$ is represented by C_p^* hereafter. The distribution of C_p^* looks similar to that of C_{pmean}. However, a detailed investigation reveals that the extent of positive C_p^* values on the external surface is somewhat narrower than that of C_{pmean}. Furthermore, the value of C_p^* in the wake region (θ >120°) is much smaller in magnitude than that of C_{pmean}, when normalized by the values at the reference point (θ = 0°). The internal pressure coefficient is nearly constant. The magnitude of C_p^* on the internal surface is larger for Model B than for Model A. The effect of roof height h_r on the C_p^* distribution can be seen in Figure 12; the effect is found to be vary small.

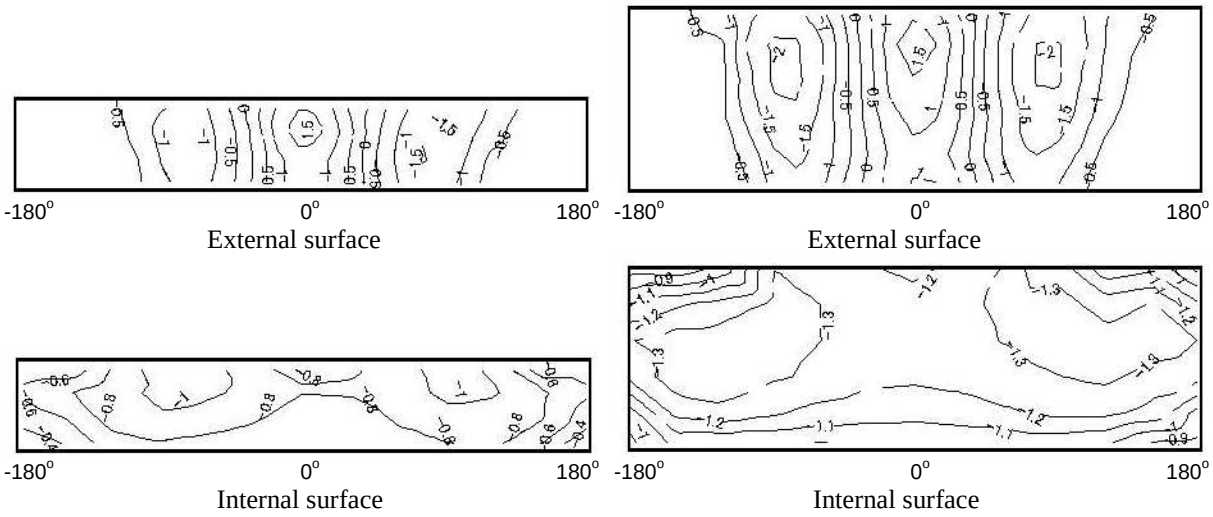

(a) Model A (b) Model B

Figure 10: The C_p distribution at the instant t_{max} when the external pressure at the reference point becomes the maximum peak value (conditional sampling).

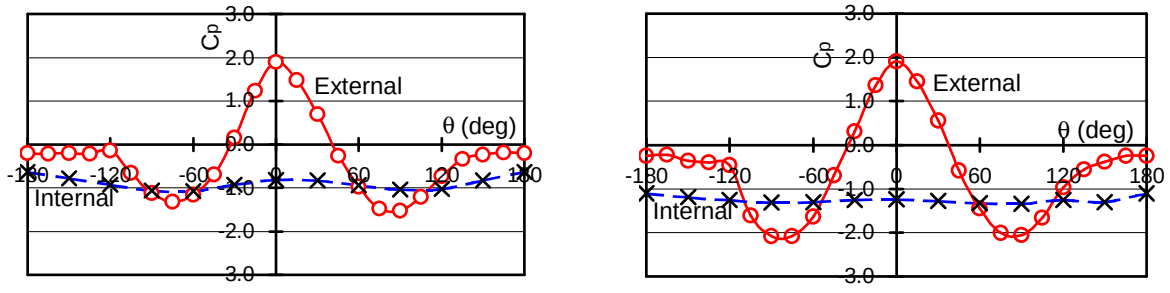

(a) Model A (z = 2/3H) (b) Model B (z = 4/5H)

Figure 11: Circumferential distribution of pressure coefficient at the instant t_{max} when the external pressure at the reference point becomes the maximum peak value (conditional sampling).

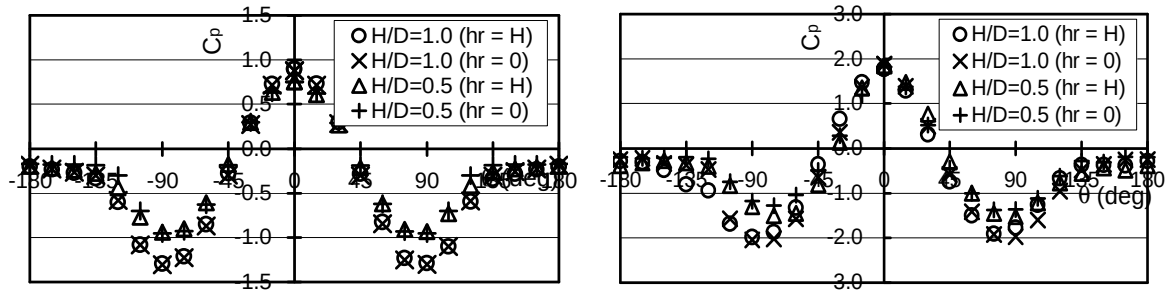

(a) Mean (b) Conditional sampling

Figure 12: Effect of roof height h_r on the distribution of external pressure coefficients at $t = t_{max}$.

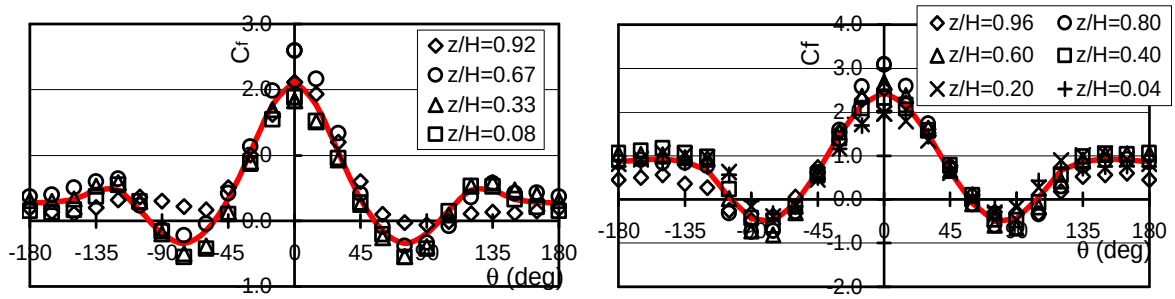

(a) Model A (b) Model B

Figure 13: Circumferential distributions of the wind force coefficient at $t = t_{max}$ ($h_r = 0$).

The circumferential distributions of wind force coefficients C_f^* at $t = t_{max}$ at various heights are shown in Figure 13. The solid line represents the average over the whole height ($z = 0 – H$), which will be used in Chapter 3. As mentioned above, the external C_p^* values in the wake region is smaller in magnitude than the corresponding C_{pmean} values, when normalized by the values at $\theta = 0^o$. Similarly, the internal C_p^* values are also smaller in magnitude than the mean internal pressure coefficients. As a result, the C_f^* distribution is close to the C_{fmean} distribution. Figure 14 shows a comparison between C_{fmean} and C_f^*, in which the averages over the whole height ($z = 0 – H$) are plotted. In the case of closed-top case, the internal pressure coefficient C_{pi} is assumed constant and equal to -0.15, which is the mean internal pressure coefficient measured in the buckling test (Section 3.1). It is interesting to note that the both distributions are close to each other, when normalized by the values at $\theta = 0^o$.

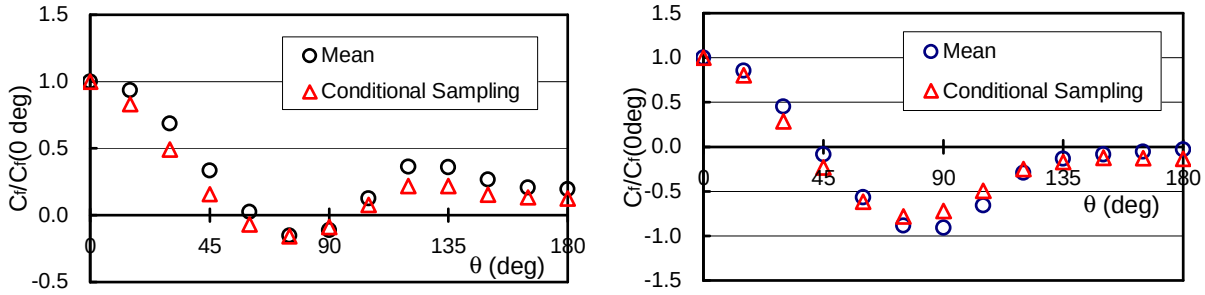

(a) Open-top ($h_r = 0$) (b) Closed-top

Figure 14: Circumferential distributions of the normalized values of C_f^* and C_{fmean} (Model A).

Shown in Figure 15 is the variation of the instantaneous C_p distribution along a circumference at $z = 2/3H$ for Model A during a period after t_{max}, where dt represents the time step of data sampling (i.e. 0.001 sec). The negative external pressures in the side and leeward regions are somewhat small in magnitude at $t = t_{max}$, but the magnitude becomes larger with time. At an instant t_{min}, the external pressure coefficient at $\theta \approx 75^o$ reaches a large negative peak value C_{ppeak}, which is equal or close to the minimum peak value C_{pmin} in the same run. The time delay $\tau = t_{min} - t_{max}$ is approximately 0.01 sec. Considering that the wind velocity U_{ref} at $z = 2/3H$ is approximately 9.3 m/s, it is found that the time delay τ roughly corresponds to the distance l ($\approx$ 93 mm) from the stagnation point ($\theta = 0^o$) to that of $\theta = 75^o$ in the leeward direction; i.e. $l \approx \tau \times U_{ref}$. This feature implies that a large-scale vortex approaching the windward stagnation point induces C_{pmax} at $\theta = 0^o$ when $t = t_{max}$. At this moment the suctions on the side region is still small. Then, this vortex induces a large suction peak C_{ppeak} at $\theta = 75^o$ when $t \approx t_{max} + \tau$, as it is shed in the leeward direction. This feature implies that the pressure field on the external surface generating the positive and negative peak values is induced by a large-scale vortex shed in the leeward direction. The internal pressure coefficient, on the other hand, does not change significantly even in this period.

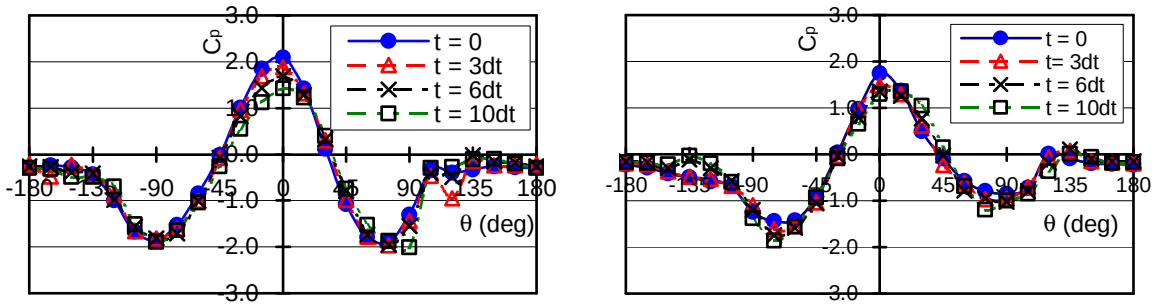

(a) Run 1 ($\tau = 10dt$) (b) Run 2 ($\tau = 10dt$)

Figure 15: Variation of the C_p distribution along a circumference at $z = 2/3H$ with time (Model A, $h_r = 0$).

2.2.3 POD analysis

Because the pressures on open-topped oil storage tanks are highly random both in time and space, a POD analysis is employed to investigate the structure of pressure field in more detail. The main objective of the POD analysis is to find a deterministic function, which is best correlated to all the elements of ensemble of a random field. In the analysis, the effect of difference in tributary area of pressure tap is considered (see Taniguchi et al. [8]).

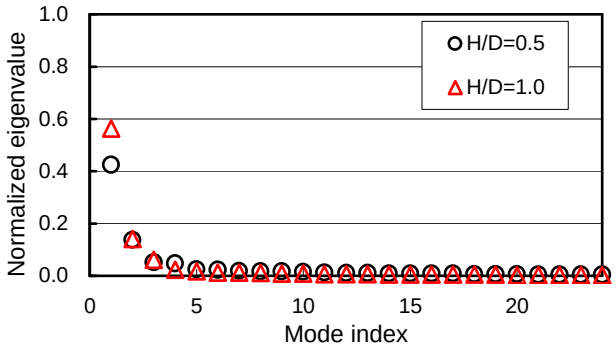

Figure 16: Normalized eigenvalues of pressures.

Figure 16 shows the normalized eigenvalues of pressures. Results on the eigenmodes for Model A are shown in Figures 17 and 18; in the figures; each eigenmode is normalized by its maximum value. The results for Model B are similar to those for Model A. The normalized eigenvalues for the first and second modes are approximately 0.5 and 0.15, respectively. Based on a two-dimensional quasi-steady assumption, the first and second mode shapes, ϕ_1 and ϕ_2, correspond to $C_{p\mathrm{mean}}$ and $\partial C_{p\,\mathrm{mean}}/\partial\theta$, respectively (see Uematsu et al. [9], for example). Figure 19 shows a comparison between the results of the POD analysis and those predicted from the quasi-steady assumption for the first and second modes, in which $C_{p\mathrm{mean}}$ and $\partial C_{p\,\mathrm{mean}}/\partial\theta$ are also normalized by their maximum values. In Figure 19(a), the results of correlation coefficient R as well as of the conditional sampling, normalized by the value at $\theta = 0^{\circ}$, are also plotted for the purpose of comparison. The results indicate that the quasi-steady assumption is valid to some degree. However, a detailed comparison reveals that the first mode shape is much similar to the C_p^* distribution obtained from the conditional sampling as well as to the distribution of the correlation coefficients.

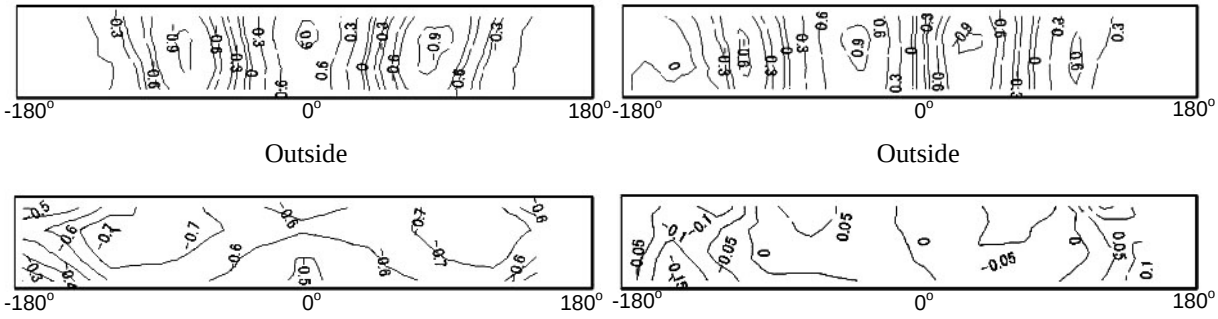

(a) First mode (b) Second mode

Figure 17: Eigenmodes of pressures on the external and internal surfaces (Model A).

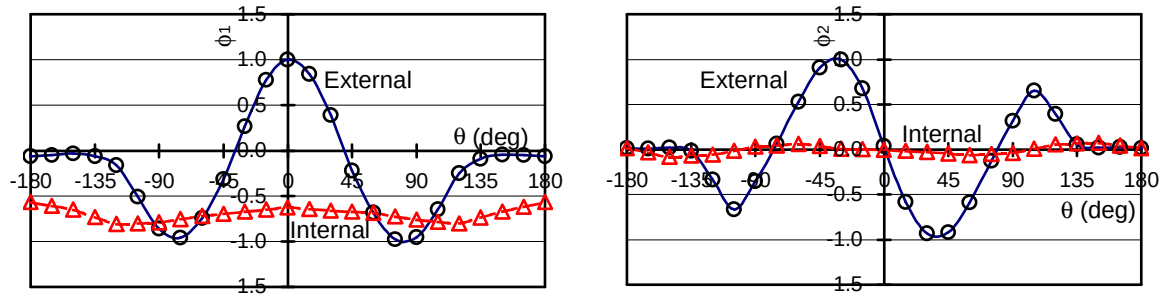

(a) First mode (b) Second node

Figure 18: Eigenmodes of pressures along a circumference at $z = 2/3H$ (Model A).

3 BUCKLING BEHAVIOR OF THIN CYLINDRICAL SHELLS

3.1 Wind tunnel experiment

Test cylinders were made of 0.1 mm thick polyester film with Young's modulus E = 5.55 GPa and Poisson's ratio ν = 0.3, by bonding a belt of 5mm width along the longitudinal seam

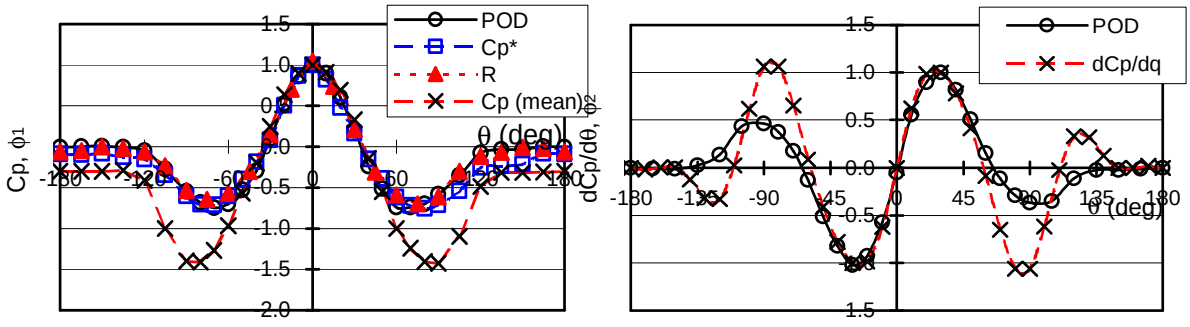

(a) First mode (b) Second mode

Figure 19: Comparison of the first and second eigenmodes with the distributions of C_{pmean} and $\partial C_{pmean}/\partial\theta$ along a circumference at $z = 2/3H$ (Model A, external pressure).

and then attaching an aluminum end plate at the bottom and an aluminum ring at the top. The belt was made of the same film as the cylinder wall. In order to obtain clear boundary conditions at the both edges, the film was bonded to a 10 mm thick end-plate at the bottom and to a ring at the top with epoxy cement (see Figure 20). The diameter D is 216 mm, and the height H is 110 mm for Cylinder A and 218 mm for Cylinder B. Therefore, the length L of the shell is 90 mm for Cylinder A and 198 mm for Cylinder B. For closed-topped cylinders, the upper ring was covered with a 1 mm thick plastic circular plate. Note that the length-to-diameter ratio (L/D) of the test cylinder is somewhat smaller than that of the height-to-diameter ratio of the models used for pressure measurements described above.

The purpose of this experiment is to discuss the relation between the wind force distribution and the buckling behavior of cylindrical shells. Therefore, the test cylinders are not modeled correctly based on any similarity law.

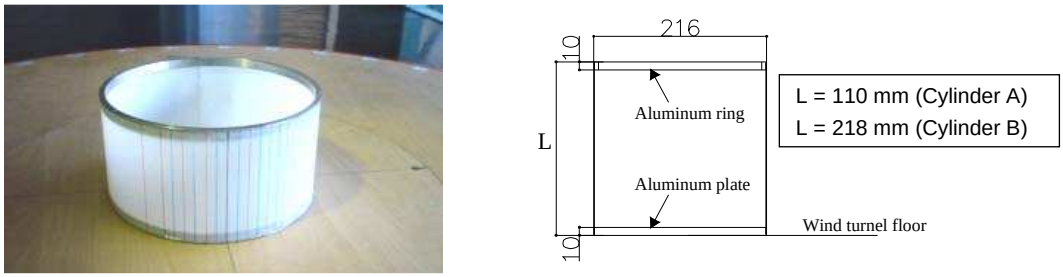

(a) Test cylinder (A) mounted in the wind tunnel (b) Dimensions of the test cylinder

Figure 20: Thin circular cylindrical shells used for the buckling test.

The experiments were carried out in an Eiffel-type wind tunnel at the Department of Architecture and Building Science, Tohoku University, which has a working section 6.5 m long, 1.4 m wide and 1.0 m high. The test cylinder with its seam at $\theta = 180^{o}$ was mounted in a turbulent boundary layer with a power law experiment of approximately 0.18. The turbulence intensity I_u is approximately 0.15 at a height of z = 110 mm and 0.11 at z = 218 mm.

As the wind speed is increased gradually, the cylinder buckles at a critical wind speed U_{Hcr}. The corresponding wind load per unit area (pressure difference) at the windward stagnation point is given by $p_{cr} = q_{Hcr}C_{fmax}$, where $q_{Hcr} = 1/2\rho U_{Hcr}^2$, with ρ being the air density, and C_{fmax} represents the wind force coefficient at the windward stagnation point; p_{cr} is simply

referred to as 'buckling load' hereafter. In the case of open-topped cylinders, the value of $C_{f\max}$ is provided from the results of the above mentioned pressure measurements (Chapter 2). For closed-topped cylinders, on the other hand, $C_{f\max}$ is provided by the difference between the maximum external pressure coefficient $C_{pe\max}$, obtained from the pressure measurements, and the internal pressure coefficient C_{pi} obtained from the buckling test. The non-dimensional buckling load λ_{cr} is defined as $\lambda_{cr} = p_{cr}R^3/D_b$, with R and D_b being the radius and flexural rigidity of the cylinder, respectively.

3.2 Theoretical analysis

Only the instability of the cylindrical shells under static wind loading is investigated, where the buckling is regarded as a bifurcation phenomenon. Taking the coordinate system as shown in Figure 21 and denoting by w and F the virtual displacement and stress function, respectively, the basic equations governing the instability of cylindrical shells may be given by Donnell as follows (see Yamaki [10], for example):

$$D_b\nabla^4 w - \frac{F_{,xx}}{R} - F_{0,yy}w_{,xx} - F_{,yy}w_{0,xx} + 2F_{0,xy}w_{,xy} + 2F_{,xy}w_{0,xy} - F_{0,xx}w_{,yy} - F_{,xx}w_{0,yy} = 0 \tag{1}$$

$$\nabla^4 F + Et\left(\frac{w_{,xx}}{R} - 2w_{0,xy}w_{,xy} + w_{0,xx}w_{,yy} + w_{,xx}w_{0,yy}\right) = 0 \tag{2}$$

$$\nabla^2 = \frac{\partial^2}{\partial x^2} + \frac{\partial^2}{\partial y^2},\ D_b = \frac{Et^3}{12(1-\nu^2)} \tag{3}$$

In these equations, w_0 and F_0 stand for the prebuckling deflection and stress function due to wind force p per unit area, respectively. The subscripts x and y preceded by commas denote differentiation with respect to the respective coordinate variables. The prebuckling deflection is so small that the values of w_0 and F_0 can be obtained from the Donnell's linear shell theory as follows:

$$D_b\nabla^4 w_0 - \frac{F_{0,xx}}{R} - p = 0 \tag{4}$$

$$\nabla^4 F_0 + \frac{Et}{R}w_{0,xx} = 0 \tag{5}$$

These equations combined with the boundary conditions can be solved by using the Galerkin method.

The wind force p is given by the product of velocity pressure q_H and wind force coefficient C_f. The circumferential distribution of C_f changes in the vertical direction. However, within the limits of the geometry under consideration here, the variation is relatively small, as shown in Figure 4. Therefore, in order to simplify the formulation, the axial variation is ignored and the averaged distribution (the solid line in Figure 4) is used. For closed-topped cylinders, the C_f distribution is provided by the averaged distribution of the external pressure coefficients C_{pe} and the constant internal pressure coefficient C_{pi} measured in the buckling test. The circumferential distribution of p can be represented by a Fourier series as follows:

$$p = q_H\left[\sum_{n=0}^{10} c_n \cos\left(\frac{ny}{R}\right)\right] \tag{6}$$

The coefficients c_n can be determined by using the least squares method applied to the experimental results.

The boundary conditions at each end of the shell are assumed as follows:

$$w = w_{,x} = u = N_{xy} = 0 \tag{7}$$

where u = virtual displacement in the axial (x) direction, and $N_{xy} = -F_{,xy}$.

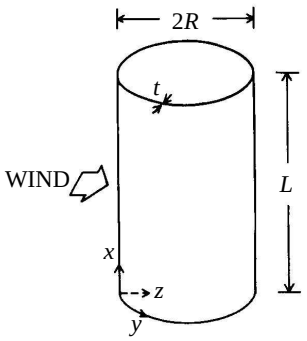

Figure 21: Notation and coordinate system of the cylindrical shell.

Buckling deflection either symmetric or antisymmetric with respect to a diametral plane parallel to the wind direction is assumed by the flowing equations:

(a) symmetric:

$$w = \sum_m \sum_n b_{mn} \left[\cos\frac{(m-1)\pi x}{L} - \cos\frac{(m+1)\pi x}{L} \right] \cos\frac{ny}{R} \quad (m = 1,\ldots,2M\text{-}1;\ n = 0,...,N) \tag{8}$$

(b) antisymmetric:

$$w = \sum_m \sum_n b_{mn} \left[\cos\frac{(m-1)\pi x}{L} - \cos\frac{(m+1)\pi x}{L} \right] \sin\frac{ny}{R} \quad (m = 1,\ldots,2M\text{-}1;\ n = 1,...,N) \tag{9}$$

The number of terms included in these approximations depends on the shell geometry. The stress function F is analytically obtained from Eq. (2). Applying the Galerkin method to Eq. (1), we can obtain a set of homogeneous linear equations in terms of the unknown parameters b_{mn}. By equating to zero the determinant of the coefficients of these equations, the buckling load p_{cr} is obtained as the least eigenvalue. Then, the values of b_{mn} corresponding to the eigen value are obtained by solving the linear equations, which give the buckling mode.

3.3 Results and discussion

Table 1 shows a comparison between experiment and theory for the non-dimensional buckling load λ_{cr}. In the wind tunnel experiments, Cylinder A with closed-top did not buckle within the limits of the maximum wind speed available. In the theoretical analysis, the numbers of M and N in Eqs. (8) and (9) are set at 2 and 40, respectively, considering the convergence of the solution. Note that the symmetric and anti-symmetric modes give the same buckling load. Figures 22 and 23 show the buckling modes for Cylinders A and B, respectively. The buckling mode was found to be approximately one wave in the axial direction in any case. On the other hand, the predominant wave number n^* in the circumferential direction depends on the shell geometry; the value of n^* increases with a

decrease in L/D. In other words, the circumferential wavelength becomes shorter, as the L/D ratio decreases. It is interesting to note that the buckling modes for open-topped and closed-topped cylinders are quite similar to each other. Furthermore, the value of n^* is almost equal to the number of circumferential waves of buckling mode when the shell is subjected to uniform lateral pressure (see Yamaki [10]). The non-dimensional buckling loads λ_{cr0} of the shells under uniform lateral pressure were also computed using the same computer program. The value of λ_{cr0} is 580 for Cylinder A and 251 for Cylinder B, which is smaller than that for the wind loading. However, the difference is not significant.

Uematsu and Uchiyama [5] proposed the following empirical formula for the non-dimensional buckling load λ_{cr} of closed-topped cylinders, based on a series of wind tunnel experiments, in which they varied the L/R ratio from 2 to 7 and the R/t ratio from 532 to 1000.

$$\lambda_{cr} = 0.83\left(\frac{L}{R}\right)^{-1.1}\left(\frac{R}{t}\right)^{0.96} \tag{10}$$

It should be mentioned that their experiments were carried out in a smooth flow, the turbulence intensity of which was less than 1 %. In the present experiment, the L/R ratio is 0.83 for Cylinder A and 1.83 for Cylinder B, and the R/t ratio is 1080 for both cylinders. The predicted results from this empirical formula are also shown in Table 1 for the purpose of comparison. The formula predicts a buckling load larger than the theoretical one, particularly for Cylinder A. This may be due to a fact that the shell geometry is out of the scope of the empirical formula.

Both the experimental and theoretical results indicate that the difference in λ_{cr} between open-topped and closed-topped cylinders is only slight despite a significant difference in the C_f distribution due to the effect of internal pressure, particularly in the side and leeward regions. This result implies that the buckling behavior of oil-storage tanks is strongly affected by the positive C_f distribution in the windward region.

The buckling loads for the C_f^* distribution obtained from the conditional sampling are also computed. In the analysis the averaged distribution of C_f^* over the whole height (solid line in Figure 13) is used. The mean internal pressure coefficient (-0.15) measured in the buckling tests is used in the closed-topped cylinder case. The results on the non-dimensional buckling loads are listed in Table 1. The buckling modes are quite similar to those for the $C_{f\text{mean}}$ distributions. As might be expected from the similarity between the $C_{f\text{mean}}$- and C_f^*-distributions (see Figure 14), the results on the buckling behavior are similar to each other.

Cylinder	Top	Experiment	Empirical formula	Theory	
				Mean C_f (n^*)	Conditional sampling (n^*)
A	open	319	–	591 (20)	618 (20)
	closed	N/A	828	614 (20)	629 (20)
B	open	241	–	295 (14)	299 (14)
	closed	245	348	310 (14)	315 (14)

Table 1 Non-dimension buckling loads λ_{cr} obtained from wind tunnel experiment, theoretical analysis and empirical formula.

The theoretical results of λ_{cr} are generally larger than the experimental values; the ratio is approximately 1.9 for Cylinder A and approximately 1.2 for Cylinder B. This feature may be related to the dynamic load effects of wind pressures on the buckling behavior. The theoretical analysis is based on the static stability of the shell. On the other hand, the wind forces on the cylinder fluctuate significantly in the wind tunnel experiment. The ratio of the

theoretical value of λ_{cr} to the experimental one is regarded as a gust effect factor G_f. The value of G_f for Cylinder A is larger than that for Cylinder B. This difference may be due to a higher turbulence of the flow and a smaller size of the test specimen for Cylinder A.

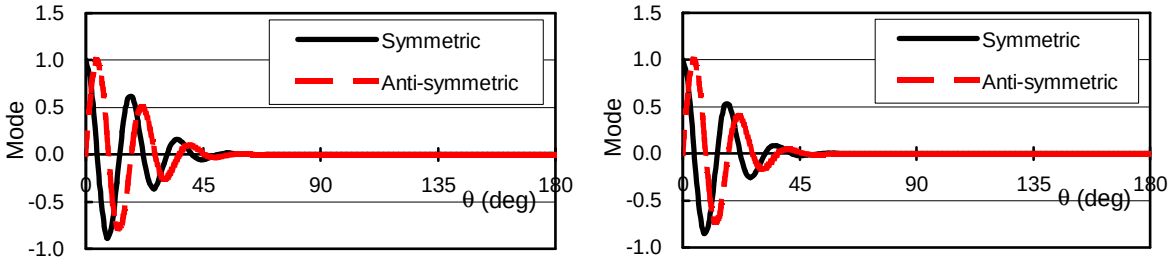

(a) Open-top (h_r = 0) (b) Closed-top

Figure 22: Buckling modes in the circumferential direction at $z = L/2$ (Cylinder A).

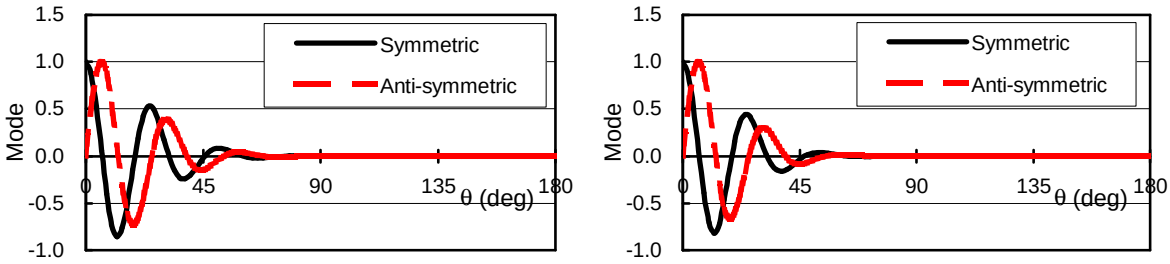

(a) Open-top (h_r = 0) (b) Closed-top

Figure 23: Buckling modes in the circumferential direction at $z = L/2$ (Cylinder B).

4 CONCLUDING REMARKS

The characteristics of wind pressures acting on open-topped oil storage tanks have been investigated in a wind tunnel. The statistical values of the external pressure coefficients change significantly in the circumferential direction. However, the variation in the axial direction is relatively small, particularly for the negative pressure coefficients in the side and wake regions. The internal pressure coefficient changes only a little both in the axial and circumferential directions. The correlation between the positive pressures on the windward stagnation point and the negative pressures in the wake region is very small, while the positive pressures are correlated to the internal pressure to some degree; the correlation coefficient ranges from approximately -0.5 to -0.6.

A conditional sampling technique gives the distribution of wind pressure and force coefficients C_p^* and C_f^* at the instant t_{max} when the external wind pressure at the reference point becomes the maximum peak value. The results indicate that the distribution of C_p^* is somewhat different from that of C_{pmean}. The C_p^* distribution is similar in shape to the first mode shape obtained from the POD analysis and to the distribution of the correlation coefficients between the pressures at the reference point and the others. In the side and leeward regions, the value of C_p^* on the external surface is smaller in magnitude than that of C_{pmean}, when normalized by the values at $\theta = 0^o$. Similarly, the value of C_p^* on the internal surface is smaller in magnitude than that of C_{pmean}. As a result, the distribution of the instantaneous wind force coefficient C_f^* at $t = t_{max}$ is similar in shape to that of the mean wind

force coefficient $C_{f\text{mean}}$. Therefore, as far as the buckling loads is concerned, the design wind force coefficient can be specified based on the mean wind force coefficients.

Experimental and theoretical analyses of the buckling of thin cylindrical shells under wind loading clearly indicate that the buckling load and mode are mainly affected by the positive wind force near the windward stagnation point. The results for open-topped cylinders are similar to those for closed-topped cylinders, despite a significant difference in the distribution of negative wind force coefficients in the side and leeward regions. The predominant wave number of buckling mode in the circumferential direction is almost the same as that for uniform lateral pressure, depending on the shell geometry (i.e. length-to-radius and radius-to-thickness ratios).

ACKNOWLEDGEMENTS

The authors are much indebted to the members of the Sub-committee for Design of Storage Tanks, Architectural Institute of Japan, for valuable discussion. Thanks are also due to Mr. Hayashida of Kajima Technical Research Institute for his help with experiments.

REFERENCES

[1] P.A. MacDonald, K.C.S. Kwok, J.D. Holmes. Wind loads on circular storage bins, silos and tanks: I. Point pressure measurements on isolated structures, *Journal of Wind Engineering and Industrial Aerodynamics*, **31**, 165–187, 1988.

[2] P.A. MacDonald, K.C.S. Kwok, J.D. Holmes. Wind loads on circular storage bins, silos and tanks: II. Effect of grouping, *Journal of Wind Engineering and Industrial Aerodynamics*, **34**, 77-95, 1990.

[3] R.J. Holroyd. On the behaviour of open-topped oil storage tanks in high winds (Part 1), *Journal of Wind Engineering and Industrial Aerodynamics*, **12**, 329-352, 1983.

[4] Y. Uematsu, M. Yamada. Aerodynamic forces on circular cylinders of finite height, *Journal of Wind Engineering and Industrial Aerodynamics*, **51**, 249-265, 1994.

[5] Y. Uematsu, K. Uchiyama. Deflection and buckling behavior of thin, circular cylindrical shells under wind loads, *Journal of Wind Engineering and Industrial Aerodynamics*, **18**, 245-261, 1985.

[6] K. Uchiyama, Y. Uematsu, T. Orimo. Experiments on the deflection and buckling behavior of ring-stiffened cylindrical shells under wind pressure, *Journal of Wind Engineering and Industrial Aerodynamics*, **26**, 195-211, 1987.

[7] Y. Uematsu, C. Koo. Wind-tunnel study of wind loads on circular cylindrical structures, *Journal of Wind Engineering*, JAWE, **33**, 17-25, 2008. (in Japanese)

[8] T. Taniguchi, Y. Taniike, H. Nishimura. POD analysis with weighted-area and time-lag for pressures on a spherical roof, Proceedings of the 14th National Symposium on Wind Engineering, Tokyo, Japan, 323-328, 1996. (in Japanese)

[9] Y. Uematsu, M. Yamada, A. Inoue, T. Hongo. Wind loads and wind-induced dynamic behavior of a single-layer latticed dome, *Journal of Wind Engineering and Industrial Aerodynamics*, **66**, 227-248, 1997.

[10] N. Yamaki. Elastic stability of circular cylindrical shells, North-Holland, Amsterdam, 1984.